# Observations of near-inertial surface currents off Oregon: Decorrelation time and length scales

Sung Yong Kim[1] and P. Michael Kosro[2]

[1]  High-resolution (km in space and hourly in time) surface currents observed by an array of high-frequency radars off Oregon are analyzed to quantify the decorrelation time and length scales of their near-inertial motions. The near-inertial surface currents are dominantly clockwise with amplitudes of 9–12 cm s$^{-1}$. However, they appear asymmetric and elliptical as a result of counterclockwise inertial motions with magnitudes in a range of 2–5 cm s$^{-1}$. The decorrelation time and length scales are computed from the decay slope of the near-inertial peak and the spatial coherence in the near-inertial frequency band, respectively. Decorrelation time scales of clockwise near-inertial motions increase from 2 days nearshore (within 30 km from the coast) to 6 days offshore, and their length scales increase from 30 to 90 km seaward possibly due to coastal inhibition. The local spatial coherence has an exponentially decaying structure for both clockwise and counterclockwise rotations, and their phases propagate northwestward (offshore) for clockwise and northeastward (onshore) for counterclockwise rotations.

## 1.  Introduction

[2]  Oscillations near the local inertial frequency are ubiquitous and intermittent phenomena in the upper ocean, driven primarily by variable wind stress, in particular, associated with moving storms and fronts with time scales of a day or two [e.g., *Pollard and Millard*, 1970; *D'Asaro*, 1985]. The momentum penetrated via the air-sea interface is converted into surface and internal inertial motions, then cascades into small scale turbulent flows through diapycnal mixing and dissipation [e.g., *Pollard and Millard*, 1970; *Gill*, 1982; *Large et al.*, 1994; *Gregg*, 1987]. The amplitudes and peak frequencies of near-inertial motions can be modified by geostrophic adjustment, background vorticity, horizontal density gradient, and tidal-inertial interactions [e.g., *Pollard*, 1983; *Kunze*, 1985a; *D'Asaro and Perkins*, 1984; *D'Asaro et al.*, 1995]. For instance, near-inertial internal waves appear to be trapped and propagated in the region of negative and positive background vorticity field, respectively, as the effective Coriolis frequency becomes subinertial and superinertial [e.g., *Kunze and Sanford*, 1984; *Kunze*, 1985a; *Weller*, 1985]. The meridional propagation of near-inertial waves is asymmetric with dominant equatorward preference [e.g., *Gill*, 1984; *Garrett*, 2001]. The near-inertial waves with positive frequency shift can horizontally propagate poleward until they reach the turning latitude (before they become subinertial waves) where they can either be reflected equatorward with their amplitudes enhanced or proceed beyond that latitude. In this meridional propagation of near-inertial waves, the beta effect causes the meridional wavelength to shorten, and those squeezed waves are prone to end up in small-scale dissipation and mixing at high latitude [e.g., *Munk*, 1981; *Fu*, 1981; *D'Asaro*, 1985; *Zhai et al.*, 2005].

[3]  Near-inertial internal motions in the coastal regions can be generated by spatially uniform and periodic wind stress, associated with shelf circulation, as well as translating wind fronts [e.g., *Gill*, 1984; *Crawford and Large*, 1996; *Davies and Xing*, 2003, 2004]. In contrast to the behavior of inertial energy in the open ocean, subsurface near-inertial oscillations are expected to be amplified offshore and decay in coastal regions due to "coastal inhibition", the downward energy flux from the surface-coast corner, that is, upward and offshore phase propagations [e.g., *Kundu*, 1976; *Millot and Crepon*, 1981; *Pettigrew*, 1981; *Flagg*, 1977; *Kundu et al.*, 1983; *Kundu*, 1984]. This has been indicated from a few mooring studies. *Webster* [1968] confirmed that the horizontal length scales of near-inertial oscillations are much larger than vertical

[1]Division of Ocean Systems Engineering, School of Mechanical, Aerospace & Systems Engineering, Korea Advanced Institute of Science and Technology, Daejeon, Republic of Korea.
[2]College of Earth, Ocean, and Atmospheric Sciences, Oregon State University, Corvallis, Oregon, USA.

Corresponding author: Sung Yong Kim, Division of Ocean Systems Engineering, School of Mechanical, Aerospace & Systems Engineering, Korea Advanced Institute of Science and Technology, 291 Daehak-ro, Guseong-dong, Yuseong-gu, Daejeon 305-701, Republic of Korea. (syongkim@kaist.ac.kr)

length scales. From observations of near-inertial currents off the Oregon coast, the horizontal coherence scales in the cross-shore direction have been episodically measured at between 60 and 120 km with their phases propagating upward and offshore at speeds of $8 \times 10^{-2}$ cm s$^{-1}$ [e.g., *Kindle*, 1974; *Johnson et al.*, 1976; *Anderson et al.*, 1983]. A differing estimate of a horizontal length scale of near-inertial motions is $O$ (10) km [*Schott*, 1971], and their downward energy propagation dominate upward propagation, as indicated by asymmetric vertical wave number spectra [e.g., *D'Asaro and Perkins*, 1984].

[4] While the vertical structure of near-inertial oscillations and their momentum transfer have been studied observationally and in numerical models [e.g., *Large et al.*, 1994, 1995; *Zervakis and Levine*, 1995; *Crawford and Large*, 1996], their horizontal length scales have been less explored due to lack of spatial observations [e.g., *Thomson and Huggett*, 1981; *D'Asaro and Perkins*, 1984; *Prandle*, 1991; *Matthews et al.*, 1993; *Shay*, 1997; *Kohut et al.*, 2006; *Rubio et al.*, 2011]. In this study, we investigate high-resolution (6 km in space and hourly in time) coastal surface currents measured by an array of high-frequency radars (HFRs), containing tides, geostrophic and ageostrophic components along with near-inertial components, to quantify the length and time scales of the near-inertial surface currents. Particularly, this paper reports an overview of averaged temporal and spatial characterization of near-inertial surface currents, based on the spectral analysis of 2 year hourly surface current observations (2007–2008). The bandwidth of near-inertial peaks in the frequency domain and the spatial coherence in the near-inertial frequency band are used to estimate the time and length scales (sections 3 and 4). In addition, the direct wind-driven near-inertial currents, the seasonal and episodic near-inertial oscillations, and variability associated with the freshwater discharge from Columbia River (CR) will be addressed in separate papers.

## 2. Observations

### 2.1. Surface Currents

[5] Hourly surface currents collected by an array of 11 shore-based HFRs operated by Oregon Sate University, from Loomis Lake, WA (46.43$^{\circ}$N) to Crescent City, CA (41.78$^{\circ}$N) for 2 years (2007–2008) are analyzed (Figure 1a). The surface vector currents and relevant kinematic and dynamic quantities (e.g., divergence, vorticity, stream function, velocity potential, and deformation rates) are directly estimated on an equally spaced grid of points with 6 km resolution using optimal interpolation. The detailed data processing technique has been reported elsewhere [e.g., *Kim et al.*, 2008; *Kim*, 2010]. The surface currents off the Oregon coast are characterized by variance at low frequency ($|\sigma| \leq 0.4$ cpd), two tidal bands at diurnal (primarily $K_1$) and semidiurnal frequencies (primarily $M_2$ and $S_2$), diurnal wind and its harmonics, as well as inertial frequency ($f_c = 1.35$–1.47 cpd for 42.5$^{\circ}$N–47.1$^{\circ}$N) [e.g., *Kim et al.*, 2011]. The hourly surface current time series are detided by least squares fitting the major tidal variance at $K_1, O_1, P_1, S_2$, and $M_2$ frequencies, but not $S_1$ frequency, because the amplitude of $S_1$ tidal currents is much weaker than that of currents driven by diurnal land/sea breezes

(e.g., National Oceanic and Atmospheric Administration, 2006. http://tidesandcurrents.noaa.gov/). There are still peaks around $K_1$ and $M_2$ frequencies because the cuspate variance due to modulation of barotropic tides with low-frequency energy exist (Figure 1b).

### 2.2. Coastal Winds

[6] The hourly wind observations are available at three National Data Buoy Center (NDBC) buoys, 46050 (W1; Stonewall bank), 46029 (W2; CR mouth), and 46041 (W3; Cape Elizabeth) (Figure 1a). The variability of coastal winds measured from NDBC buoys off the U.S. West Coast (USWC) is dominated by subinertial alongshore winds and diurnal variability [e.g., *Koracin et al.*, 2004; S. Y. Kim, Revisiting local and remote wind-coherent responses of sea surface heights off the U.S. West Coast, submitted to *Ocean Dynamics*, 2013]. The principal axes of coastal winds are parallel to the shoreline.

### 2.3. Note on Spectral Analysis

[7] The spectral analysis applied in this paper is based on the finite Fourier transform instead of using multitaper method [e.g., *Elipot et al.*, 2010]. A single time series is divided into $M$ nonoverlapped time series with identical $N$ record lengths in order that the estimates have degrees of freedom (DOF; 2 $M$) at a reasonable confidence level. If the missing data are more than 30% of the length of each segment of time series, that segment is not included in the following computation (the data less than 70% of hourly observations are excluded). The fractional data availability ($\beta$) of surface currents to participate in the analysis is shown in Figure 1e. The estimates of the confidence interval are based on the chi-square distribution [*von Storch and Zwiers*, 1999; see section 4 for more details]. On the other hand, the temporal variation of near-inertial energy in the study domain is examined with surface current time series within an overlapped moving time window in order to present continuous variability (Figure 4 and section 3).

## 3. Near-Inertial Coastal Surface Currents

### 3.1. Near-Inertial Variance

[8] The averaged rotary power spectrum of detided surface currents over the Oregon coast shows dominant clockwise variance and relatively weak counterclockwise energy (Figure 1b), which implies horizontally asymmetric and elliptical motions of near-inertial surface currents instead of pure circular motions.

[9] The amplitude of surface currents at the local inertial frequency ($f_c$) is computed by least squares fitting (Figure 1c). Each segment of surface current time series is fitted with the local inertial frequency where the data are sampled (section 2.3). On the other hand, the amplitude of near-inertial surface currents is a square root of the sum of the area below the energy spectrum between two enhanced peaks at $K_1$ and $M_2$ frequencies (Figures 1b and 1d). The bandwidth of near-inertial frequency band varies with coastal regions. The alongshore distribution of the amplitudes of inertial and near-inertial surface currents off the USWC are presented in Figures 1c and 1d, respectively, for
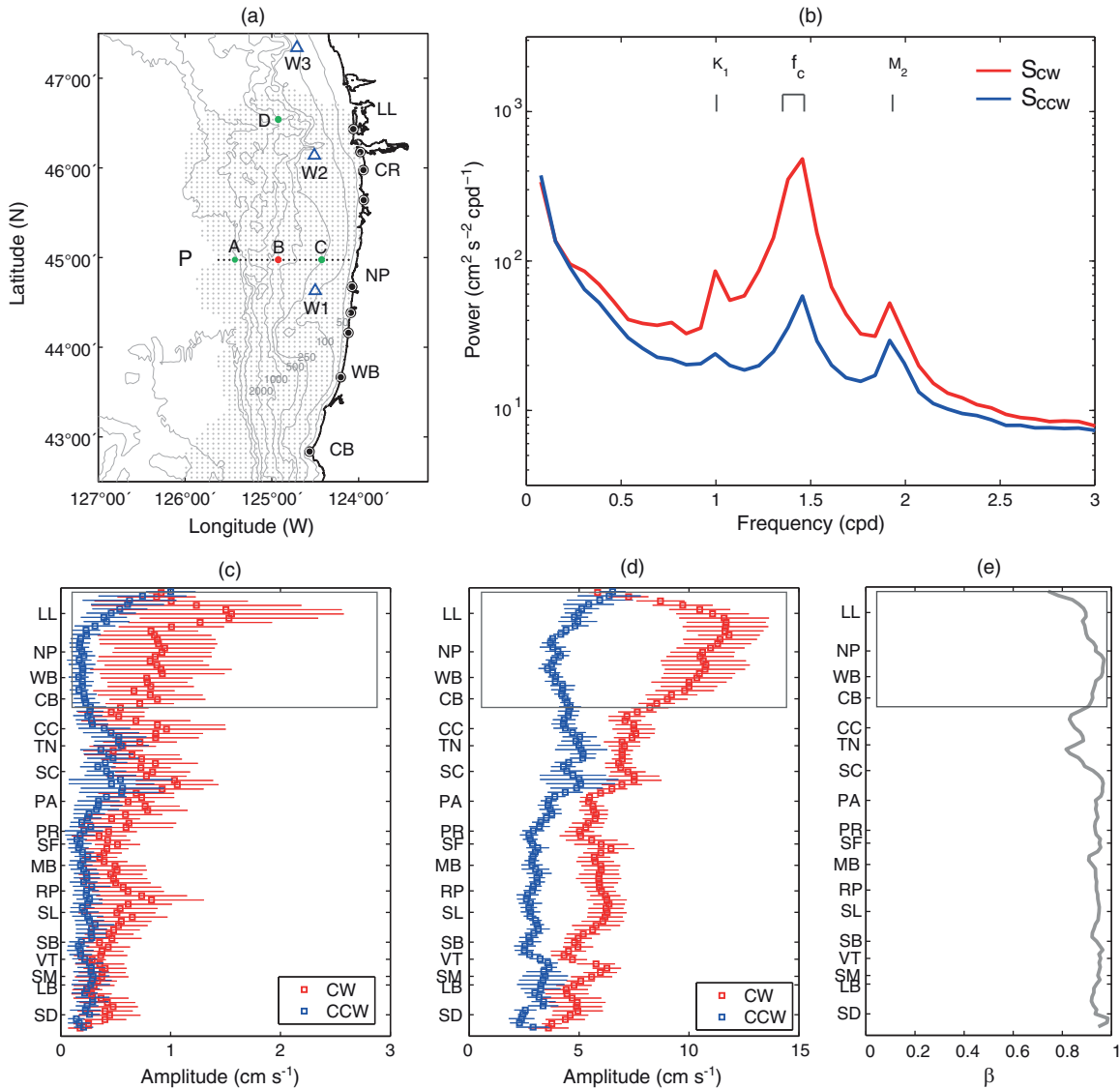
**Figure 1.** (a) Study area for near-inertial surface currents off Oregon and southern Washington. A gray dotted area denotes the effective spatial coverage at least 90% data availability. Blue triangles (W1, W2, and W3) and dots indicate the NDBC wind buoys (46050, 46029, and 46041) and HFRs, respectively. The estimates of decorrelation time and length scales are presented with examples on grid points A, B, and C along a cross-shore line P and the grid point D. The bottom bathymetry is contoured with 50, 100, 250, 500, 1000, and 2000 m. (b) Regionally averaged rotary power spectra of detided surface currents off Oregon and southern Washington. (c and d) The range of local inertial frequencies and $K_1$ and $M_2$ frequencies are indicated. Alongshore distribution of the amplitudes of surface currents over the large-scale U.S. West Coast (USWC) (c) at the local inertial frequency (d) in the near-inertial frequency band is presented as the mean (square) and standard deviation (error bar). (e) The fractional data availability ($\beta$) of only participating surface currents over two years in the computation, adapted from *Kim et al.* [2011]. For reference, the locations of some coastal regions along the USWC are denoted by abbreviated two letter names: San Diego (SD), Long Beach (LB), Santa Monica (SM), San Buenaventura (VT), Santa Barbara Channel (SB), Port San Luis (SL), Ragged Point (RP), Monterey Bay (MB), San Francisco (SF), Point Reyes (PR), Point Arena (PA), Shelter Cove (SC), Trinidad (TN), Crescent City (CC), Cape Blanco (CB), Winchester Bay (WB), Newport (NP), Columbia River (CR), and Loomis Lake (LL). A gray box in Figures 1c–1e indicates the region of Oregon and southern Washington, shown in Figure 1a.

clockwise and counterclockwise rotations. For the along-shore presentation of the near-inertial amplitude, a coast-line axis is designed as a spline curve having 20 km resolution following the coastline. All grid points in the study domain are mapped into the axis to make a set of grid points in the cross-shore direction corresponding to a single
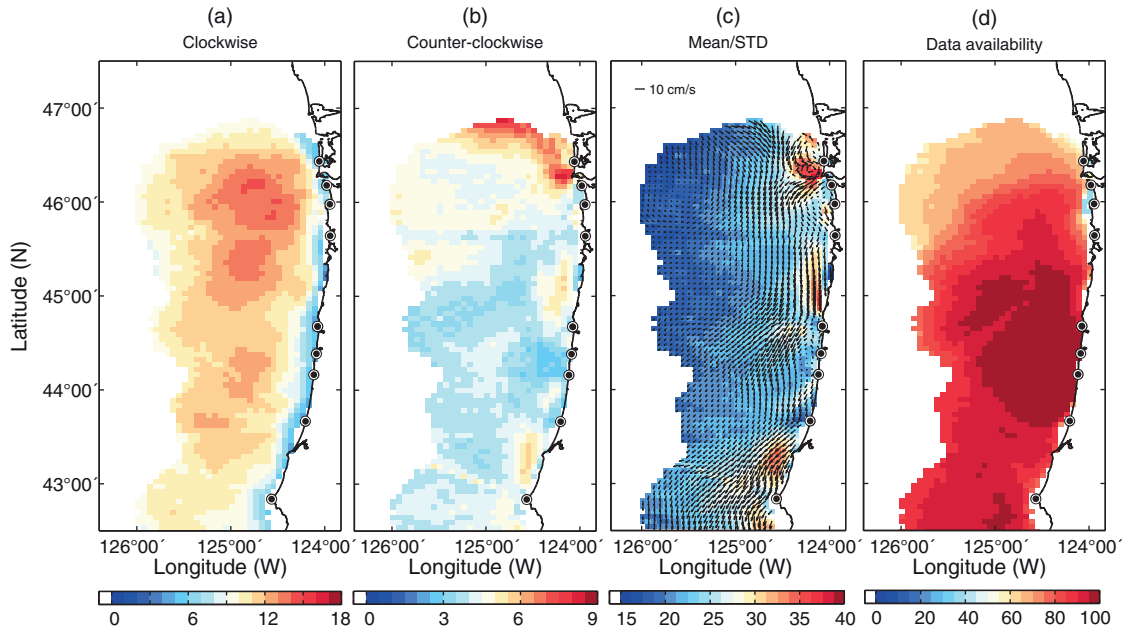
**Figure 2.** Amplitudes (cm s$^{-1}$) of near-inertial surface currents in (a) clockwise and (b) counterclockwise directions. (c) Mean (arrows) and standard deviation (STD; colors) (cm s$^{-1}$) of hourly surface currents over two years (2007–2008). (d) Data availability of hourly surface currents over two years (2007–2008).

location on the axis. The amplitudes estimated from surface vector currents at each grid point are classified into a similar way, then their mean and standard deviation (STD) are shown as a square and horizontal bar, respectively [e.g., *Kim et al.*, 2011].

[10] The amplitudes of near-inertial surface currents show a tendency to increase with latitude. This increase may be from both intermittently persistent (e.g., multiple step functions) and strong winds as well as the energetic nonlinear interactions due to smaller baroclinic Rossby deformation radius and greater intermittency (Figure 1d) [e.g., *Munk and Phillips*, 1968; *Stammer*, 1997; *Chelton et al.*, 1998]. The amplitudes of inertial and near-inertial surface currents are weakly sensitive to missing observations (Figure 1e). Another data set for two years (2009–2010) shows a consistent amplitude distribution in the alongshore direction. In the cross-shore direction, near-inertial variance of surface currents has the minimum near the coast and becomes enhanced from 20 km offshore, and its peak gets narrowed along with the transition to pure inertial motions (Figure 2 and see *Kim et al.* [2011] for more details).

[11] The amplitudes at the inertial frequency are approximately five times less than those in the near-inertial frequency band in this study (Figures 1c and 1d). The inertial motions in the real ocean are ubiquitously observed at the slightly higher frequency than the local inertial frequency ($\sigma \rightarrow f_c$) [e.g., *Kundu*, 1976], which is referred to as near-inertial motions as a result of their interactions with low-frequency energy and background vorticity (e.g., mesoscale or submesoscale eddies) [e.g., *Mooers*, 1975; *Kunze*, 1985a; *Paduan et al.*, 1989; *Jones*, 2001; *Elipot et al.*, 2010]. For instance, the effective Coriolis frequency ($f_e$) is

equal to the planetary Coriolis frequency ($f_c$) plus half of the relative vorticity ($\zeta$):

$$f_e = \left[ f_c^2 + f_c \left( \frac{\partial V}{\partial x} - \frac{\partial U}{\partial y} \right) - \frac{\partial V}{\partial x} \frac{\partial U}{\partial y} - \frac{\partial U}{\partial x} \frac{\partial V}{\partial y} \right]^{\frac{1}{2}}, \quad (1)$$

$$\approx f_c + \frac{1}{2} \left( \frac{\partial V}{\partial x} - \frac{\partial U}{\partial y} \right) = f_c + \frac{\zeta}{2}, \quad (2)$$

where $U$ and $V$ denote the time mean or low-frequency current components in the $x$- and $y$ directions [*Kunze*, 1985a, as corrected in *Kunze*, 1985b]. Thus, the pure-inertial variance may not well capture the near-inertial motions and can underestimate them [e.g., *Park et al.*, 2004].

[12] The amplitudes of near-inertial surface currents off Oregon are shown in Figures 2a and 2b. Clockwise energy is most dominant offshore from the CR and maintains over 10 cm s$^{-1}$ (Figure 2a). However, this is also the edge of radar coverage and may have lowered reliability. Gently reduced clockwise variance is found near the coast. This appears to be a "coastal inhibition" [e.g., *Flagg*, 1977; *Pettigrew*, 1981; *Kundu et al.*, 1983; *Kundu*, 1984]. Counterclockwise variance is enhanced in two nearshore areas, north of Newport (NP) and Cape Blanco (CB) (Figure 2b). In the Northern Hemisphere, inertial currents dominantly rotate clockwise. However, as the currents can be rectilinear near the coast, the clockwise and counterclockwise near-inertial variance is expected to be nearly equal, which can be speculated as a result of the coastal reflection of near-inertial waves or bottom trapped waves [e.g., *Rhines*, 1970; *Jordi and Wang*, 2008; *Chen et al.*, 1996]. In particular, the reflection of near-inertial waves from the continental slope or the coast can produce a superposition of incident and reflected
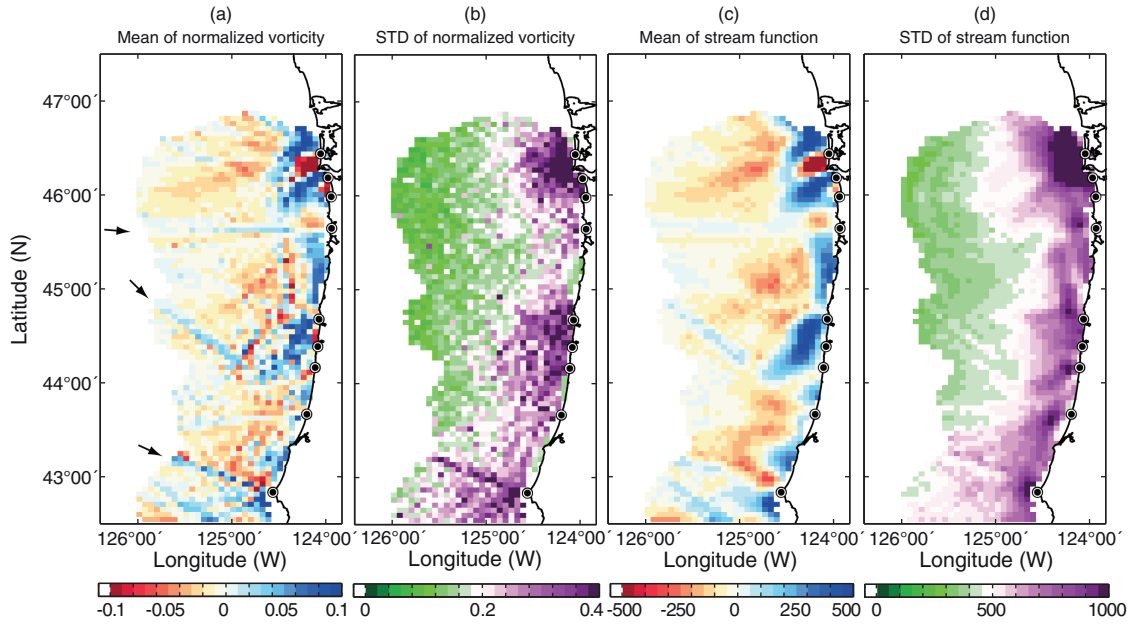
**Figure 3.** Mean and standard deviation (STD) of normalized vorticity $(\zeta/f_c)$ and stream function $(\psi; \mathrm{m^2\,s^{-1}})$ derived from surface currents over two years (2007–2008). Negative and positive values indicate clockwise and counterclockwise directions, respectively. Black arrows in (a) indicate spurious estimates along the azimuthal bins of individual radar sites.

waves, which can cause the counterclockwise components near the bottom or in the subsurface [e.g., *Jordi and Wang*, 2008; *Chen et al.*, 1996; *Martini et al.*, 2011].

[13] In this paper, the analysis was conducted on surface currents with at least 70% data availability over 2 years; the highest availability (90%) appears in the middle of the study domain (Figure 2d).

### 3.2. Time Mean of Surface Currents and Vorticity

[14] The time mean and STD of surface currents over two years (2007–2008) are shown in Figure 2c. Offshore mean surface currents are mainly southward and southeastward.

[15] The mean and STD of normalized vorticity $(\zeta/f_c)$ and stream function $(\psi)$ derived from surface currents are shown in Figure 3. In the estimates of vorticity and stream function, the isotropic exponential function with 10 km decorrelation length scales in the $x$ and $y$ directions is used (see *Kim* [2010] and *Kim et al.* [2011] for more details). The stream function has been used as a proxy to identify the areas of high Rossby number (normalized vorticity; $R_o = U/f_c L \approx \zeta/f_c$, where $U$ and $L$ are the current speed and length scale, respectively) because the spatial structure of the stream function is relatively smoother than the vorticity field and the sign of rotation of both quantities are almost same [e.g., *Kim*, 2010]. Thus, the use of stream function is convenient to analyze the maps with vortical features without extra spatial filtering. The primary vortical features off Oregon are clockwise offshore and counterclockwise onshore (within 30 km from the shoreline) resulting from the equatorial coastal jet and local eddies and meanders nearshore due to coastal boundaries. The averaged normalized vorticity varies within $\pm 0.1$ and its STD becomes significant in three nearshore regions (CR, NP, and CB).

[16] Due to shifting of the effective Coriolis frequency by the background vorticity, we might expect the clockwise inertial peak in the offshore area to move to superinertial frequency due to the reinforcing clockwise background vorticity (Figure 3a). Onshore, the positive background vorticity can modulate the counterclockwise inertial motions by shifting the peak to superinertial counterclockwise frequencies.

[17] There are several places to have anomalous mean and STD related to bias in antenna beam patterns (Kosro and Kim, in preparation). They are identified with the mean and STD of radial velocities at individual radar sites, and appear in several azimuthal bins having spatially incoherent STD, indicated with black arrows in Figure 3a: CBL1 (293°), MAN1 (269°), and WIN1 (315°) where the angles are measured from the true north in the clockwise direction. Those are visible in the near-inertial amplitudes, mean and STD of their vector currents as well (Figure 2). However, this spatial bias is less than 3% of total number of grid points, and the overall results in the paper were not influenced by those artifacts.

### 3.3. Near-Inertial Variance in Time

[18] Wind forcing is characterized by the daily averaged alongshore wind time series at NDBC 46050, 46029, and 46041 buoys in Figure 4 (see Figure 1a for buoy locations). The missing observations are estimated objectively using the sample data covariance matrix obtained from hourly wind observations at 15 NDBC wind buoys off the USWC for 16 years (1995–2010). The gridded data are presented with paler colors in Figure 4a. The alongshore winds have STD of 7–9 m s$^{-1}$ and several high wind events appear during winter (2007–2008).

[19] Regionally averaged rotary power spectra of surface currents are presented as a function of time for clockwise
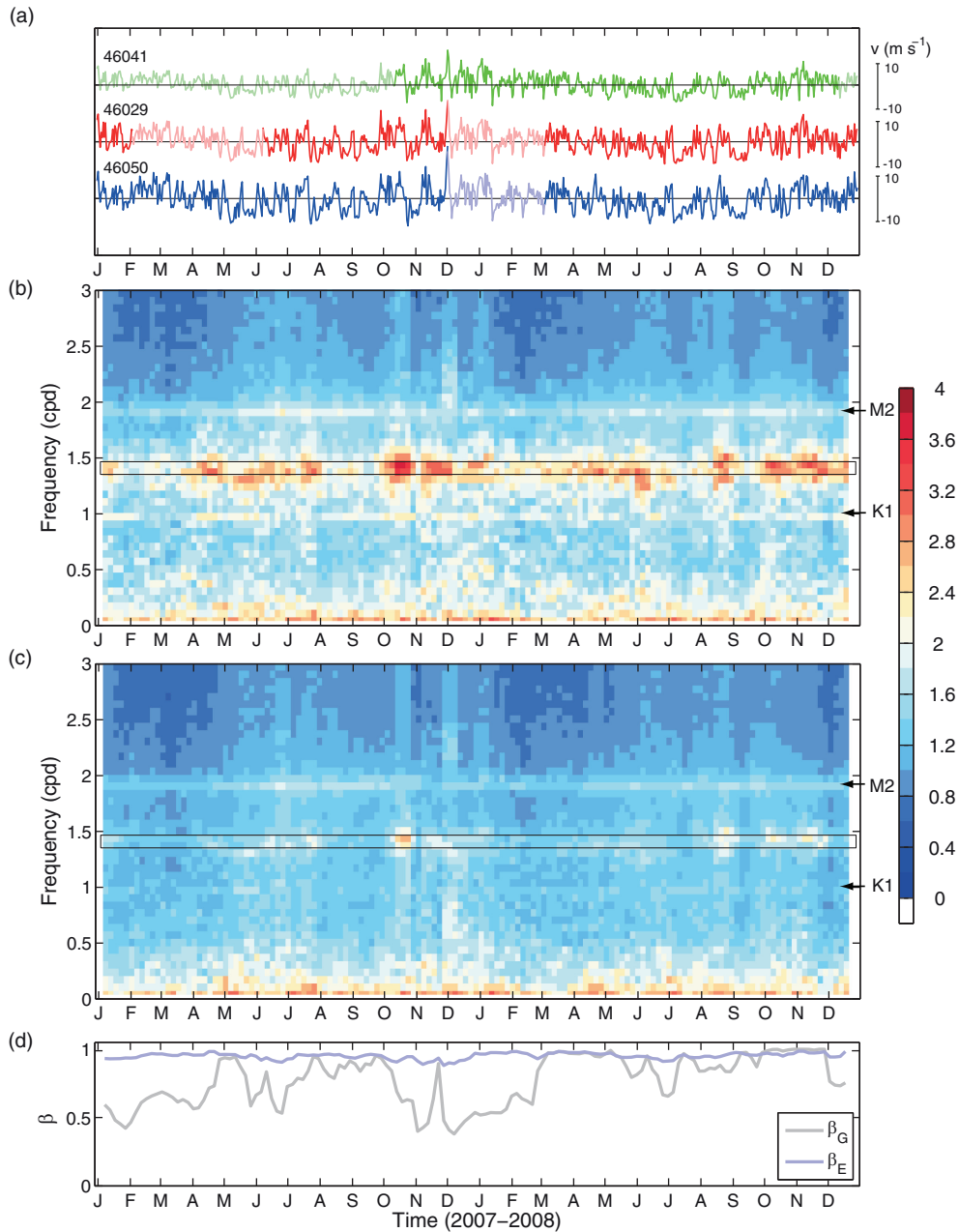
**Figure 4.** (a) Daily averaged alongshore wind velocity (m s$^{-1}$) at NDBC 46050 (W1), 46029 (W2), and 46041 (W3) buoys. The missing data are gridded with sample data covariance matrix obtained from hourly wind observations at 15 NDBC buoys off the USWC for 16 years (1995–2010). The hourly gridded data are presented with paler colors. (b and c): Averaged spectrogram of detided surface currents $\left(\mathrm{cm}^2\mathrm{s}^{-2}\mathrm{cpd}^{-1}, \log_{10} \text{ scale}\right)$ off Oregon. Variance at major tidal frequencies ($M_2, K_1, O_1, S_2, N_2,$ and $P_1$) is removed. Note that residual variance at diurnal ($S_1$) and semidiurnal ($M_2$) frequencies still remains. Individual spectra are estimated with time series within 15 day time window with a 5 day increment. The black rectangular boxes indicate the range of local Coriolis frequency. (d) The ratio ($\beta_G$) of the number of grid points to be used in the estimate of rotary spectra to total grid points in Figure 1a and the fractional data availability ($\beta_E$) of chosen surface currents time series.

(Figure 4b) and counterclockwise (Figure 4c) rotations. Individual spectra are computed from surface current time series within 15 day long moving time window with a 5 day increment. The time series with more than 20% missing data (less than 80% observations) within 15 day long records are not included. We defined two indicators as function of time to present the quality and availability of the data to participate the spectra estimate. $\beta_G$ is a fraction of the number of grid points relative to the total grid points in the domain, and $\beta_E$ is a fraction of observations relative to the total record length within the moving time window (Figure 4d).

**(a)**
**Decorrelation time scales**

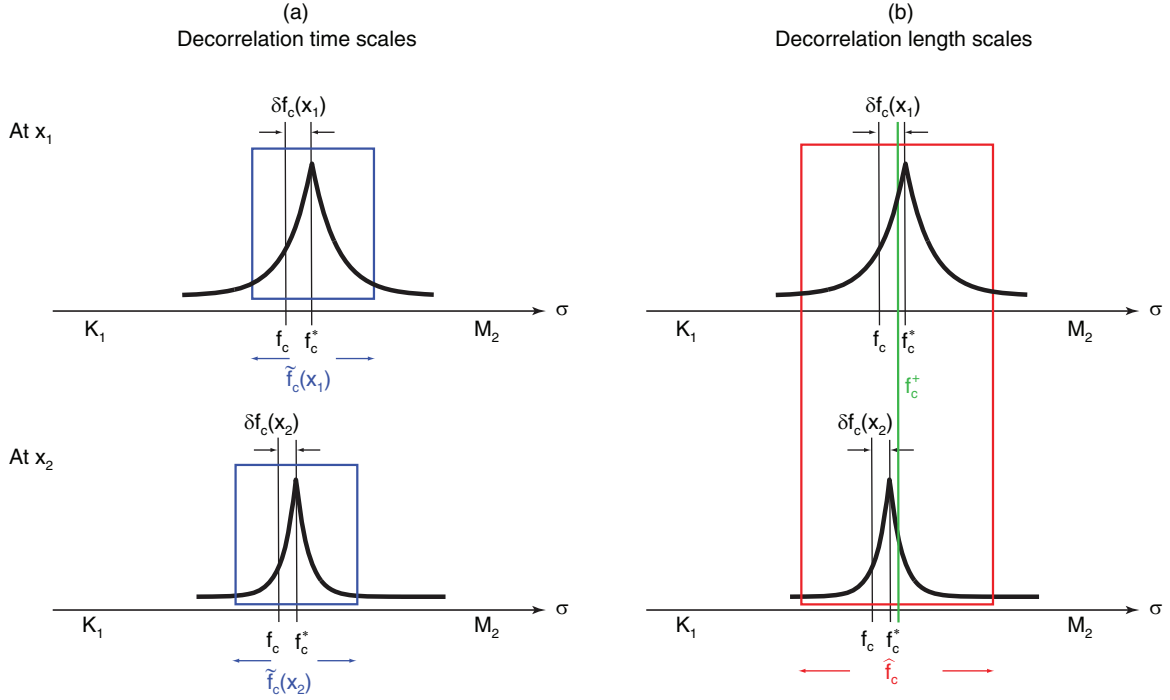**(b)**
**Decorrelation length scales**

**Figure 5.** A schematic presentation of two near-inertial frequency bands [$\tilde{f}_c$ as blue boxes in (a); $\hat{f}_c$ as a red box in (b)] using power spectra of near-inertial surface currents at two locations ($\mathbf{x}_1$ and $\mathbf{x}_2$). The peak inertial frequency $\left(f_c^*\right)$ is a sum of the local inertial frequency ($f_c$) and a deviation ($\delta f_c$). For the estimate of decorrelation time scales, a frequency band $\tilde{f}_c$, centered by $f_c^*$ as a function of space ($\mathbf{x}$), is considered. On the other hand, decorrelation length scales are computed from coherence in a frequency band ($\hat{f}_c$), which covers near-inertial variance in two locations. The center frequency ($f_c^+$; a green line in (b)) is the nearest frequency to the average of two local Coriolis frequencies [$f_c(\mathbf{x}_1)$ and $f_c(\mathbf{x}_2)$].

[20] While clockwise near-inertial energy has seasonality with greatest energy during late fall and early winter, it appears episodically over most of the year (Figure 4b). On the other hand, counterclockwise near-inertial variance is much smaller than clockwise (Figure 4c). The low-frequency variance in both rotations is almost equivalent. Some high wind events and spatially averaged clockwise inertial variance appear to be coherent. Particularly, the directly wind-forced near-inertial responses will be examined in a separate paper. Another data set in other time periods (2009–2010) shows a similar tendency of seasonality and recurring near-inertial variance year round. The residual variance at diurnal and semidiurnal frequencies and low-frequency energy (less than 0.4 cpd) is also present in the same way.

## 4. Estimates of Decorrelation Scales

[21] Here we estimate the decorrelation scales in time and space with spectral analysis. The decorrelation time and length scales are computed from the decay slope of the peak (section 4.1) and the spatial coherence (section 4.2) in the near-inertial frequency band, respectively. The decay slope of the peak can be estimated from the spectra at individual grid points. On the other hand, the spatial coherence should be taken into account in pairs of two grid points. Thus, the near-inertial frequency bands can be defined in slightly different ways ($\tilde{f}_c$ and $\hat{f}_c$) (Figure 5).

### 4.1. Decorrelation Time Scales

[22] The peak frequency $\left(f_c^*\right)$ within the near-inertial frequency band $\left(\tilde{f}_c\right)$ is the frequency having the maximum magnitude of Fourier coefficients, computed by fitting a series of trial frequencies in a band of $f_c \pm 0.2$ cpd with an increment of 0.002 cpd [e.g., *Shay et al.*, 1998].

[23] The deviation ($\delta f_c$) from a local inertial frequency ($f_c$) is

$$\delta f_c = f_c^* - f_c. \qquad (3)$$

[24] Thus, a near-inertial frequency band $\left(\tilde{f}_c\right)$ is centered by the peak frequency $\left(f_c^*\right)$ with a bandwidth ($n$)

$$\tilde{f}_c = f_c^* \pm n\Delta\sigma, \qquad (4)$$

where $\Delta\sigma$ is the frequency bin ($n$ is integer) defined for a time series with $N$ evenly sampled records from $t_1$ to $t_N$,

$$\Delta\sigma = \frac{N-1}{N}\frac{1}{t_N - t_1}. \qquad (5)$$

[25] A single time series is divided into the nonoverlapped time series with identical record lengths, and the Fourier coefficients of each chunk of surface current time series are computed. When the 2 year hourly time series are divided into $M$ ensembles ($M = 56, \Delta\sigma = 0.0767$ cpd),
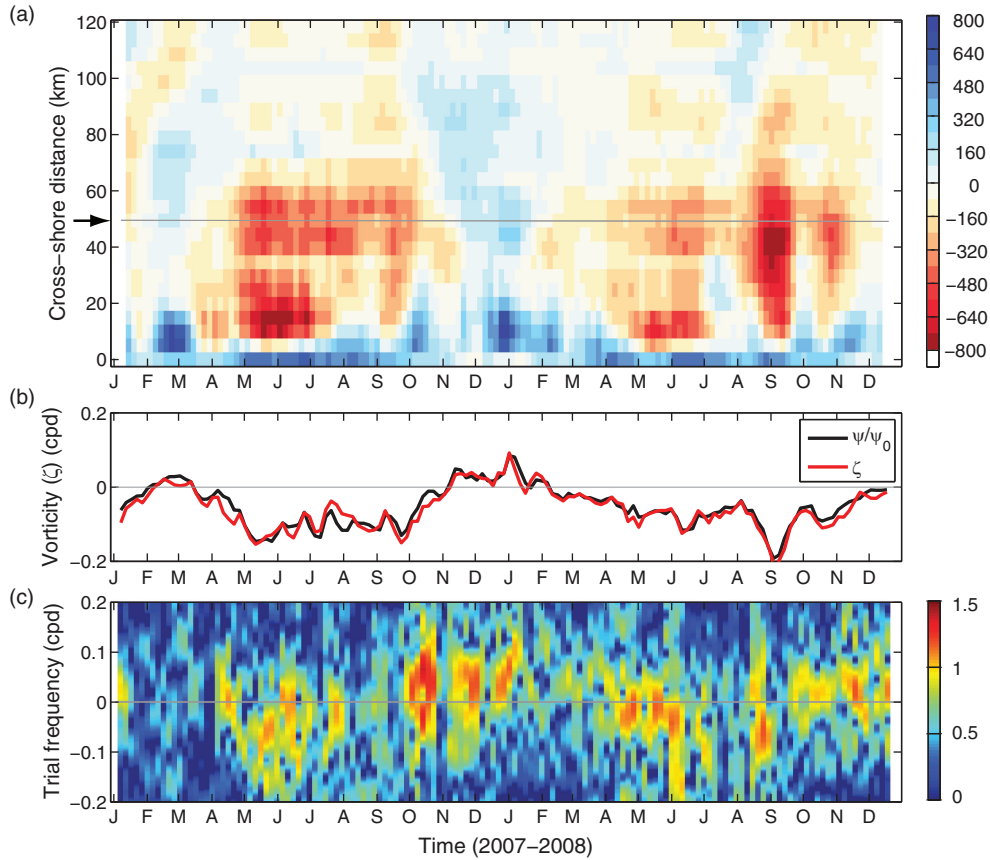
**Figure 6.** (a) Time evolution of stream function ($\psi$; m$^2$ s$^{-1}$) along a grid line P in Figure 1a. (b) Time evolution of vorticity ($\zeta$, cpd) and scaled stream function ($\psi/\psi_0, \psi_0 = 4000$ m$^2$ s$^{-1}$) at the grid point B in Figure 1a. (c) Clockwise variance (cm$^2$ s$^{-2}$, log$_{10}$ scale) of surface currents at trial frequencies, centered by the local inertial frequency ($f_c = 1.4136$ cpd).

the range of the peak inertial frequency is $-1.51 \leq f_c^* \leq -1.3575$ cpd in clockwise and $1.158 \leq f_c^* \leq 1.591$ cpd in counterclockwise rotations, respectively.

[26] The near-inertial frequency band $(\hat{f}_c)$ can be expanded as long as it does not include residual variance at $K_1$ and $M_2$ frequencies. However, a constant bandwidth ($n = 3$) is chosen to consistently estimate time scales of surface currents within the domain.

[27] The individual power spectra within $\hat{f}_c$ are approximated with a $\sigma^{-2}$ function and a decay slope ($\lambda$) (equation (6)) in order to quantify the decorrelation time scale ($\lambda$) (equation (7)).

$$S(\sigma) = \frac{A^2 \lambda^2}{1 + \lambda^2 \left(\sigma + f_c^*\right)^2}, \qquad (6)$$

$$c(t) = A e^{-i f_c^* t} e^{-\frac{t}{\lambda}}, t \geq 0 \qquad (7)$$

where $A$ is the constant amplitude in the time domain.

[28] As the peak frequencies of individual power spectra can vary with background vorticity, the fitting with equation (6) should be conducted by following shifted peaks. The time evolution of the stream function ($\psi$) along a cross-shore grid line P (Figure 1a) shows that the normalized vorticity or rotational tendency is mainly clockwise

nearshore (within 10 km from shoreline) and alternates between counterclockwise during winter and spring and clockwise during summer and fall in the offshore region (Figure 6a). Figure 6b presents time series of vorticity ($\zeta$) and scaled stream function ($\psi/\psi_0; \psi_0 = 4000$ m$^2$ s$^{-1}$) at a grid point B (50 km offshore; Figure 1a), indicated with a black arrow in Figure 6a. Both quantities vary seasonally. In order to present an example of the frequency shift of the inertial peak due to background vorticity, variance of surface currents at trial frequencies (within 0.2 cpd of local inertial frequency) is computed and presented as a function of time in Figure 6c. Although the shifted amount from $f_c$ is not completely the half of background vorticity ($\zeta$), their tendency in time indicates the influence of local vorticity. While vorticity propagations in the cross-shore direction can be identified (Figure 6a), they are not addressed in the scope of this paper.

[29] The clockwise decorrelation time scales vary from 2 (nearshore) to 6 (offshore) days (Figure 7a). Coastal inhibition due to coastline and bottom friction are considered as primary causes of the shorter decay time scale of nearshore near-inertial surface currents [e.g., *Kundu*, 1976; *Millot and Crepon*, 1981; *Pettigrew*, 1981; *Kundu*, 1984]. The decorrelation time scales of counterclockwise near-inertial surface currents are not well determined due to low signal-to-noise ratio (SNR) (Figure 7b). Despite the low SNR, the
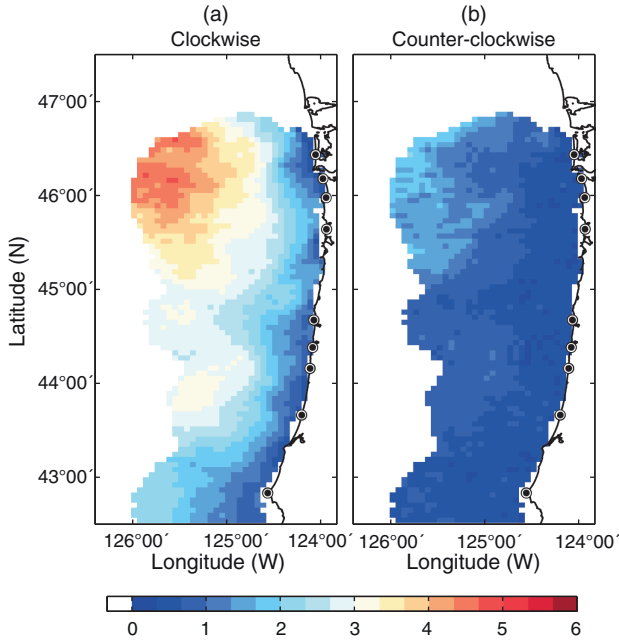
**Figure 7.** Decorrelation time scales (days) of (a) clockwise and (b) counterclockwise near-inertial surface currents.

counterclockwise near-inertial time scales are much shorter than clockwise ones, which is expected in the Northern Hemisphere. As a complimentary way to determine the decorrelation time scale, the data-derived and model-derived wind transfer functions can be considered.

### 4.2. Decorrelation Length Scales

[30] The decorrelation length scales of near-inertial surface currents are examined with spatial coherence, regarded as the spatial correlation within a specific frequency band:

$$\hat{c}(\Delta\mathbf{x}, \hat{f}_c) = \frac{\langle \hat{\mathbf{u}}(\mathbf{x}, \hat{f}_c) \, \hat{\mathbf{u}}^{\dagger}(\mathbf{x} + \Delta\mathbf{x}, \hat{f}_c) \rangle}{\sqrt{\langle |\hat{\mathbf{u}}(\mathbf{x}, \hat{f}_c)|^2 \rangle} \sqrt{\langle |\hat{\mathbf{u}}(\mathbf{x} + \Delta\mathbf{x}, \hat{f}_c)|^2 \rangle}}, \quad (8)$$

where $\hat{\mathbf{u}}$ is the Fourier coefficients of vector current time series and $\langle \cdot \rangle$ indicates averaging over the near-inertial frequency band $(\hat{f}_c)$. To estimate the spatial coherence of near-inertial surface currents at two grid points, a common near-inertial frequency band should be determined (Figure 5b). Although the same bandwidth in both rotations could be applied as was done for the time scale estimate (Figure 5a), that may not guarantee that basis functions of Fourier coefficients computed at two different locations are orthogonal. Thus, the near-inertial frequency band $(\hat{f}_c)$ (Figure 5b) for coherence estimates is defined from the finite frequency axis (Appendix A):

$$\hat{f}_c = f_c^+ \pm m\Delta\sigma, \quad (9)$$

where a reference frequency $(f_c^+)$ is the nearest frequency to the inertial frequency averaged at two locations

$(\mathbf{x}$ and $\mathbf{x} + \Delta\mathbf{x})$. Note that the changes in $f_c^*$ within the estimation window are ignored.

[31] The bandwidth $(m)$ is determined in a range where the frequency window is not overlapped with tides (e.g., $K_1$ and $M_2$). $\hat{f}_c$ corresponds to $f_c^+ \pm 0.3067$ cpd in clockwise $(m = 4)$ and $f_c^+ \pm 0.1534$ cpd in counterclockwise rotations $(m = 2)$. The reference frequency varies between $1.3524 \leq |f_c^+| \leq 1.4659$ cpd $(M = 56, \Delta\sigma = 0.0767$ cpd$)$. As bandwidth $(m)$ gets bigger, the magnitude of coherence becomes reduced rapidly. However, the shape of spatial coherence is less sensitive to the size of bandwidth. The same bandwidth in both rotations can be applicable when the time scale is estimated. However, as the reduction of coherence in the counterclockwise rotation becomes significant due to low SNR, so half of the bandwidth in the clockwise rotation is chosen for the counterclockwise bandwidth. As the local inertial frequencies at two locations may not be typically the same $[f_c(\mathbf{x}_1) \neq f_c(\mathbf{x}_2)]$, the spatial coherence between two locations is computed from off-centered frequency band. As a worst case, when two grid points are separated meridionally by 100 km, the difference of center frequencies becomes 0.03 cpd $[|f_c(\mathbf{x}) - f_c(\mathbf{x} + |\Delta\mathbf{x}|)| = 0.03$ cpd $< \Delta\sigma]$. Thus, as long as the decorrelation length scales are less than 100 km, the difference between center frequencies involved in the computation of coherence can be ignored because it is less than the size of the frequency bin $(\Delta\sigma)$.

[32] Spatial coherence of near-inertial surface currents between a given reference location and other grid points is presented with its amplitude and phase (Figure 8). Two grid points (A and C in Figure 1a) on the grid line P and a grid point (D in Figure 1a) in the northern edge are chosen to highlight the spatial structure and phase propagation of near-inertial surface currents with clockwise (Figures 8a, 8c, 8e, 8g, 8i, and 8k) and counterclockwise (Figures 8b, 8d, 8f, 8h, 8j, and 8l) rotations, respectively.

[33] The amplitude of spatial coherence shows that the decorrelation length scales of clockwise near-inertial surface currents are much larger (stay above 0.5) for the clockwise (20–80 km) than the counterclockwise (~10 km, not much longer than the 6 km measurement grid) rotating currents, depending on the distance from the shoreline (Figures 8a, 8e, and 8i). However, there are regions where clockwise and counter-clockwise near-inertial surface currents have more comparable length scales, for instance, in the north of CR and nearshore regions (Figures 8i and 8j).

[34] The phase map indicates propagating features of near-inertial oscillations in terms of the propagating direction and wavelength. As clockwise variance is more dominant than counterclockwise variance off the Oregon coast (Figure 2), the phase maps of clockwise motions tend to be better organized than those of counterclockwise ones (third and fourth columns in Figure 8, respectively). Northwestward phase propagation can be seen offshore for the clockwise component, reaching points A and C (Figures 8c and 8g), and northeastward propagation can be seen nearshore for the counterclockwise component, reaching point D (Figure 8l). These correspond to horizontal propagation of near-inertial oscillations with wavelength of 1000–1200 km (clockwise) and 300–400 km (counterclockwise).
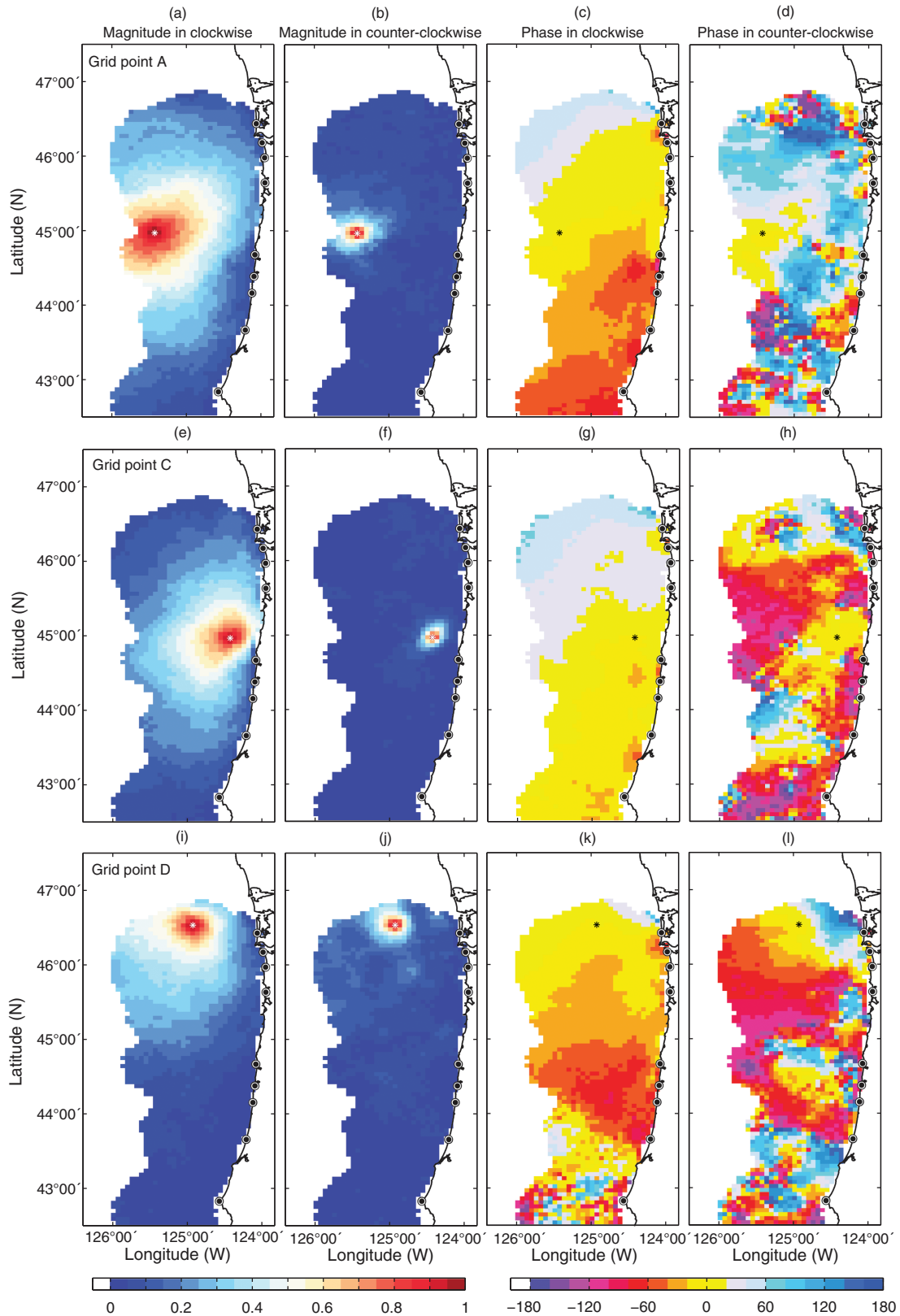
**Figure 8.** Magnitude and phase (degrees) of coherence of near-inertial surface currents relative to a reference location (A, C, and D in Figure 1a presented with white or black stars). First column: clockwise magnitude; second column: counterclockwise magnitude; third column: clockwise phase; fourth column: counterclockwise phase. The magnitude is averaged over the near-inertial frequency band, and the phase is computed from a single frequency bin nearby two near-inertial peaks. (a–d) Grid point A. (e–h) Grid point C. (i–l) Grid point D.
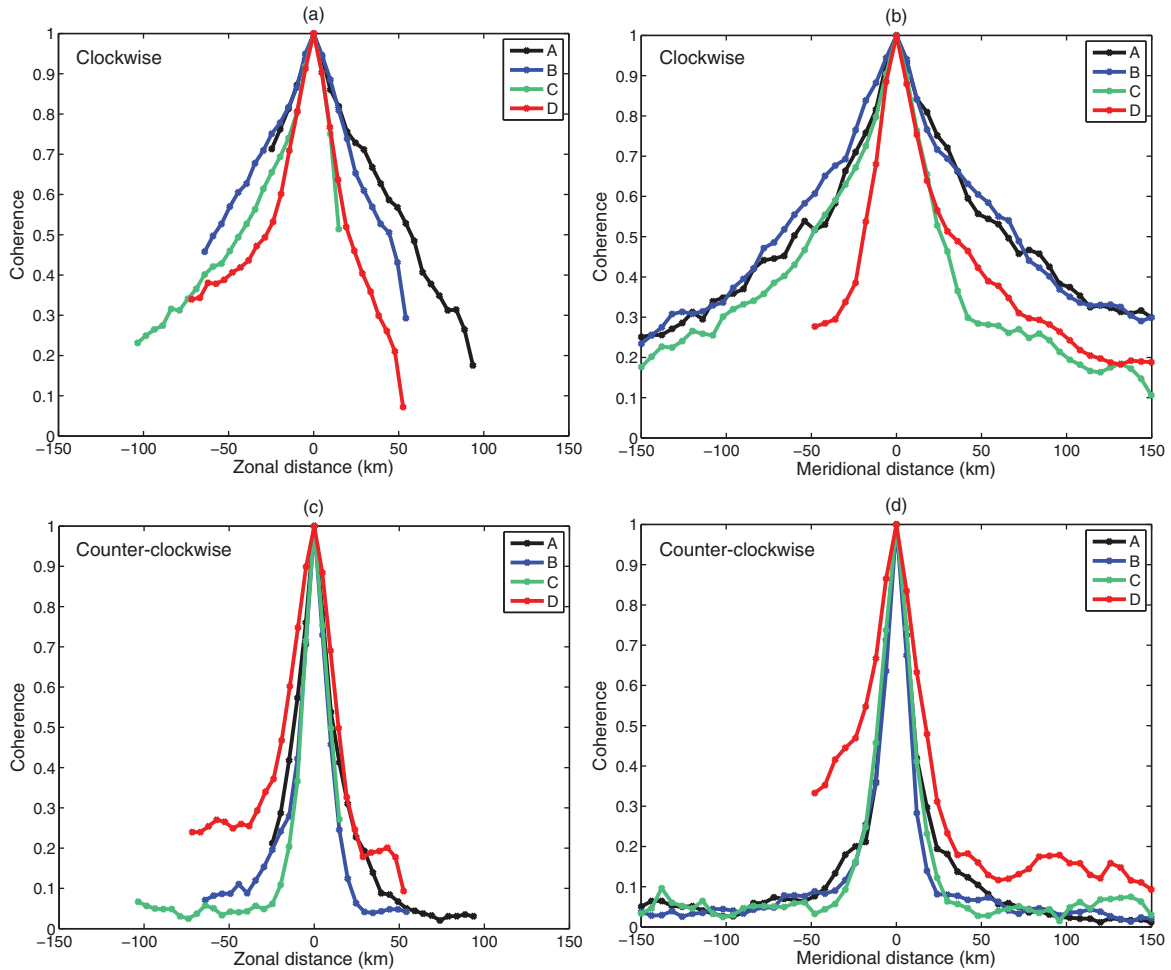
**Figure 9.** (a and c) Zonal and (b and d) meridional cross sections of the magnitude of coherence at four grid points (A, B, C, and D in Figure 1a). (a and b) Clockwise direction. (c and d) Counterclockwise direction.

[35] All phase maps contain partially northward propagations [e.g., *Müller et al.*, 1978; *Anderson and Gill*, 1979], which can be caused by a blue shift of near-inertial variance (Figures 3a, 3c, and 6a). The clockwise and counterclockwise inertial variance turns into superinertial variance due to negative (mostly offshore) and positive (within 15 km from the coast in the north of CR) local relative vorticity (Figure 6b), respectively. Subsurface near-inertial oscillations in coastal regions tend to be amplified and to decay rapidly due to coastal inhibition, as a downward flux from the surface-coast corner, that is, upward and offshore phase propagations. [e.g., *D'Asaro*, 1985; *D'Asaro et al.*, 1995; *Zhai et al.*, 2005].

[36] Two-dimensional zonal and meridional cross-sections of spatially lagged coherence magnitudes centered by the reference grid points tend to decay exponentially rather than in a Gaussian manner (Figure 9). The amplitudes of coherence over grid points within a 15 km radius from a reference point are compositely averaged in the spatial lag domain in order to increase the DOF of estimates and to yield the smooth local structure. The locally averaged amplitudes are fitted with an exponential function

[e.g., *Kim*, 2009]. The length scales of clockwise near-inertial surface currents increase from 30 to 90 km seaward (Figure 10). However, the spatial scales of the counterclockwise surface currents are 40%–60% less than the clockwise ones. The decreasing tendency of length scales nearshore may result from coastal inhibition.

## 5. Summary and Discussion

[37] The decorrelation scales of near-inertial surface currents observed by an array of HFR off the Oregon coast have been investigated. The decorrelation time and length scales are computed from the decay slope of the near-inertial peak and the spatial coherence in the near-inertial frequency band, respectively. In order to increase DOF, a single time series of surface currents is divided into nonoverlapped time series with identical record lengths, and spectral estimates are based on their ensemble average. As the inertial peak is shifted with background vorticity, the decay slopes of the peak are computed following the peak in each chunk of the time series. Decorrelation time scales of clockwise near-inertial motions increase from nearshore (within 30 km from the coast) to offshore from 2 to 6 days,
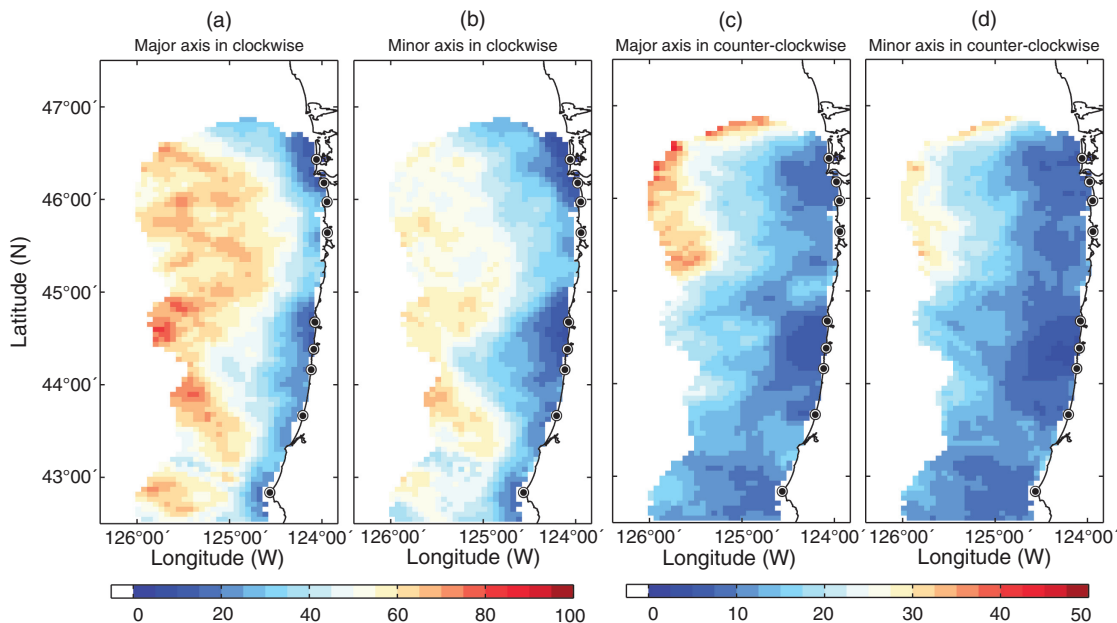
**Figure 10.** Decorrelation length scales (km) of near-inertial surface currents ($\hat{f}_c$), fitted into an exponential function. (a and b) Length scales on major and minor axes in the clockwise direction. (c and d) Length scales on major and minor axes in the counterclockwise direction.

and their length scales have a similar spatial tendency increasing from 30 to 90 km seaward. The spatial coherence has an exponentially decaying structure for both rotations and their phases propagate northwestward (offshore) in clockwise and northeastward (onshore) in counterclockwise rotations. The northeastward phase propagation in the counterclockwise rotation is only observed at the northern domain. These partially poleward propagations may be caused by the positively shifted near-inertial currents due to positive vorticity near the coast. The beta-dispersion effect predicts that near-inertial internal waves are free to propagate equatorward (northward phase propagation), but are restricted in their poleward propagation by the planetary vorticity gradient [e.g., *Anderson and Gill*, 1979; *Gill*, 1984].

[38] The near-inertial surface currents are dominantly clockwise with amplitudes of 9–12 cm s$^{-1}$ and appear as asymmetric and elliptical as a result of counterclockwise inertial motions with magnitudes in a range of 2–5 cm s$^{-1}$. Reduced clockwise variance is found in nearcoast areas, possibly as a result of coastal inhibition, which is a downward flux from the surface-coast corner (upward and offshore phase propagations). Although the inertial currents in the Northern Hemisphere dominantly rotate clockwise, the reflection of near-inertial waves from the continental slope or the coast can produce a superposition of the incident and reflected waves, which can cause the counterclockwise components [e.g., *Jordi and Wang*, 2008; *Martini et al.*, 2011]. In particular, the currents can be rectilinear near the coast, so the clockwise and counterclockwise near-inertial variance is expected to be nearly equal [e.g., *Gonella*, 1972], which can be speculated as a result of the coastal reflection of near-inertial waves or bottom trapped waves

[e.g., *Rhines*, 1970; *Chen et al.*, 1996]. The bandwidth of the peak may be related to the low-frequency cross-shore pressure gradients or coastal influence such as bottom topography and shoreline constraints of no normal flow.

## Appendix A: Frequency Axis

[39] The evenly sampled data ($d(t_n)$) are discrete Fourier transformed into $\hat{d}(\sigma_k)$:

$$\hat{d}(\sigma_k) = \frac{1}{N}\sum_{n=0}^{N-1} d(t_n)e^{-i\sigma_k t_n}, \tag{A1}$$

where $\sigma_k = 2\pi f_k$.

[40] In the finite time series with discrete, continuous, and evenly sampled $N$ records, the finite frequency axis is defined as

$$f_k = \Delta\sigma(k - N^* - 1), \tag{A2}$$

where $N^* = \lfloor N/2 \rfloor (k = 1, 2, \cdots, N)$. $\lfloor \cdot \rfloor$ denotes the greatest integer function (or floor function): $\lfloor x \rfloor = \max\{m \in \mathcal{Z} | m \leq x\}$.

research organizations on the USWC: Scripps Institution of Oceanography at University of California, San Diego, University of Southern California, Marine Science Institute at University of California, Santa Barbara, California Polytechnic State University, Naval Postgraduate School, Romberg Tiburon Center at San Francisco State University, Humboldt State University, Bodega Marine Laboratory at University of California, Davis, and Oregon State University. The three USWC IOOS regional coastal ocean observing systems—SCCOOS, CeNCOOS, and NANOOS—are acknowledged for their continued support and advocacy of HFR current measurements for monitoring the oceans. The wind data are from the National Data Buoy Center (NDBC).

# References

Anderson, D. L., and A. E. Gill (1979), Beta dispersion of inertial waves, *J. Geophys. Res.*, *84*(C4), 1836–1842.

Anderson, I., A. Huyer, and R. Smith (1983), Near-inertial motions off the Oregon coast, *J. Geophys. Res.*, *88*(C10), 5960–5972.

Chelton, D. B., R. A. DeSzoeke, M. G. Schlax, K. E. Naggar, and N. Siwertz (1998), Geophysical variability of the first baroclinic Rossby radius of deformation, *J. Phys. Oceanogr.*, *28*, 433–460.

Chen, C., R. Reid, and W. Nowlin Jr. (1996), Near-inertial oscillations over the Texas-Louisiana shelf, *J. Geophys. Res.*, *101*(C2), 3509–3524.

Crawford, G. B., and W. G. Large (1996), A numerical investigation of resonant inertial response of the ocean to wind forcing, *J. Phys. Oceanogr.*, *26*, 873–891.

D'Asaro, E. A. (1985), The energy flux from the wind to the near-inertial motions in the surface mixed layer, *J. Phys. Oceanogr.*, *15*, 1043–1059.

D'Asaro, E. A., and H. Perkins (1984), A near-inertial internal wave spectrum for the Sargasso Sea in late summer, *J. Phys. Oceanogr.*, *14*(3), 489–505.

D'Asaro, E. A., C. C. Ericksen, M. D. Levine, P. Niiler, C. A. Paulson, and P. V. Meurs (1995), Upper-ocean inertial currents forced by a strong storm Part I: Data and comparison with linear theory, *J. Phys. Oceanogr.*, *25*, 2909–2936.

Davies, A., and J. Xing (2003), Processes influencing wind-induced current profiles in near coastal stratified regions, *Cont. Shelf Res.*, *23*(14–15), 1379–1400.

Davies, A., and J. Xing (2004), Wind-induced motion in the vicinity of a bottom density front: Response to forcing frequency, *J. Geophys. Res.*, *109*, C09002, doi:10.1029/2003JC002151.

Elipot, S., R. Lumpkin, and G. Prieto (2010), Modification of inertial oscillations by the mesoscale eddy field, *J. Geophys. Res.*, *115*, C09010, doi:10.1029/2009JC005679.

Flagg, C. N. (1977), The dynamics and kinematics of the coastal boundary layer off Long Island, Ph.D. thesis, Mass. Inst. of Technol., Dep. of Meteorol., Cambridge, Mass. [Available at http://hdl.handle.net/1721.1/52836.]

Fu, L. (1981), Observations and models of inertial waves in the deep ocean, *Rev. Geophys.*, *19*(1), 141–170.

Garrett, C. (2001), What is the near-inertial band and why is it different from the rest of the internal wave spectrum? *J. Phys. Oceanogr.*, *31*(4), 962–971.

Gill, A. E. (1982), *Atmosphere-Ocean Dynamics, Int. Geophys. Ser.*, vol. *30*, 662 pp., Academic Press, New York, N. Y.

Gill, A. E. (1984), On the behavior of internal waves in the wakes of storms, *J. Phys. Oceanogr.*, *14*, 1129–1151.

Gonella, J. (1972), A rotary-component method for analysis in meteorological and oceanographic vector time series, *Deep Sea Res.*, *19*, 833–846.

Gregg, M. (1987), Diapycnal mixing in the thermocline: A review, *J. Geophys. Res.*, *92*(C5), 5249–5286.

Johnson, W., J. Van Leer, and C. Mooers (1976), A cyclesonde view of coastal upwelling, *J. Phys. Oceanogr.*, *6*(4), 556–574.

Jones, R. M. (2001), The dispersion relation for internal acoustic-gravity waves in a baroclinic fluid, *Phys. Fluid*, *13*, 1274–1280.

Jordi, A., and D. Wang (2008), Near-inertial motions in and around the Palamós submarine canyon (NW Mediterranean) generated by a severe storm, *Cont. Shelf Res.*, *28*(17), 2523–2534.

Kim, S. Y. (2009), Coastal ocean studies in southern San Diego using high-frequency radar derived surface currents, Ph.D. thesis, Scripps Inst. of Oceanogr., Tech. Rep., La Jolla, Calif. [Available at http://escholarship.org/uc/item/2z5660f4.]

Kim, S. Y. (2010), Observations of submesoscale eddies using high-frequency radar-derived kinematic and dynamic quantities, *Cont. Shelf Res.*, *30*, 1639–1655, doi:10.1016/j.csr.2010.06.011.

Kim, S. Y., E. J. Terrill, and B. D. Cornuelle (2008), Mapping surface currents from HF radar radial velocity measurements using optimal interpolation, *J. Geophys. Res.*, *113*, C10023, doi:10.1029/2007JC004244.

Kim, S. Y. (2011), Mapping the U.S. West Coast surface circulation: A multiyear analysis of high-frequency radar observations, *J. Geophys. Res.*, *116*, C03011, doi:10.1029/2010JC006669.

Kindle, J. (1974), The horizontal coherence of inertial oscillations in a coastal region, *Geophys. Res. Lett.*, *1*(3), 127–130.

Kohut, J. T., S. M. Glenn, and J. D. Paduan (2006), Inner shelf response to tropical storm Floyd, *J. Geophys. Res.*, *111*, C09S91, doi:10.1029/2003JC002173.

Koracin, D., C. E. Dorman, and E. P. Dever (2004), Coastal perturbations of marine-layer winds, wind stress, and wind stress curl along California and Baja California in June 1999, *J. Phys. Oceanogr.*, *34*, 1152–1173.

Kundu, P. J. (1976), An analysis of inertial oscillations observed near Oregon coast, *J. Phys. Oceanogr.*, *6*, 879–893.

Kundu, P. K. (1984), Generation of coastal inertial oscillations by time-varying wind, *J. Phys. Oceanogr.*, *14*(12), 1901–1913.

Kundu, P. K., S.-Y. Chao, and J. P. McCreary (1983), Transient coastal currents and inertio-gravity waves, *Deep Sea Res.*, *30*(10), 1059–1082, doi:10.1016/0198-0149(83)90061-4.

Kunze, E. (1985a), Near-inertial wave propagation in geostrophic shear, *J. Phys. Oceanogr.*, *15*, 544–565.

Kunze, E. (1985b), Near-inertial wave propagation in geostrophic shear: Corrigendum, *J. Phys. Oceanogr.*, *15*, 1355–1356.

Kunze, E., and T. Sanford (1984), Observations of near-inertial waves in a front, *J. Phys. Oceanogr.*, *14*(3), 566–581.

Large, W., J. McWilliams, and S. Doney (1994), Oceanic vertical mixing: A review and a model with a non-local boundary layer parameterization, *Rev. Geophys.*, *32*(4), 363–403.

Large, W. G., J. Morzel, and G. B. Crawford (1995), Accounting for surface wave distortion of the marine wind profile in low-level ocean storms wind measurements, *J. Phys. Oceanogr.*, *25*, 2959–2971.

Martini, K., M. Alford, E. Kunze, S. Kelly, and J. Nash (2011), Observations of internal tides on the Oregon continental slope, *J. Phys. Oceanogr.*, *41*, 1772–1794, doi:10.1175/2011JPO4581.1.

Matthews, J., A. Fox, and D. Prandle (1993), Radar observation of an along-front jet and transverse flow convergence associated with a North Sea front, *Cont. Shelf Res.*, *13*(1), 109–130.

Millot, C., and M. Crepon (1981), Inertial oscillations on the continental shelf of the Gulf of Lions: Observations and theory, *J. Phys. Oceanogr.*, *11*, 639–657.

Mooers, C. N. K. (1975), Several effects of baroclinic currents on the three-dimensional propagation of inertial-internal waves, *Geophys. Fluid Dyn.*, *6*, 277–284.

Müller, P., D. Olbers, and J. Willebrand (1978), The IWEX spectrum, *J. Geophys. Res.*, *83*(C1), 479–500.

Munk, W. (1981), Internal waves and small scale processes, in *Evolution of Physical Oceanography*, chap. 9, p. 623, MIT Press, Cambridge, Mass.

Munk, W. H., and N. Phillips (1968), Coherence and band structure of inertial motion in the sea, *Rev. Geophys.*, *6*(4), 447–472.

Paduan, J. D., R. de Szoeke, and R. A. Weller (1989), Inertial oscillations in the upper ocean during the Mixed Layer Dynamics Experiment (MILDEX), *J. Geophys. Res.*, *94*, 4835–4842.

Park, J., K. Kim, and W. Crawford (2004), Inertial currents estimated from surface trajectories of ARGO floats, *Geophys. Res. Lett.*, *31*, L13307, doi:10.1029/2004GL020191.

Pettigrew, N. R. (1981), The dynamics and kinematics of the coastal boundary layer off Long Island, Ph.D. thesis, Mass. Inst. of Technol., Dep. of Meteorol. and Phys. Oceanogr., Cambridge, Mass. [Available at http://hdl.handle.net/1721.1/27913.]

Pollard, R. (1983), Observations of the structure of the upper ocean: Wind-driven momentum budget, *Philos. Trans. R. Soc. London Ser. A Math. Phys. Sci.*, *308*(1503), 407–425.

Pollard, R. T., and R. C. Millard (1970), Comparison between observed and simulated wind-generated inertial oscillations, *Deep Sea Res.*, *17*, 813–821.

Prandle, D. (1991), A new view of near-shore dynamics based on observations from HF radar, *Prog. Oceanogr.*, *27*(3), 403–438.

Rhines, P. (1970), Edge-, bottom-, and Rossby waves in a rotating stratified fluid, *Geophys. Fluid Dyn.*, *1*, 273–302.

Rubio, A., G. Reverdin, A. Fontán, M. González, and J. Mader (2011), Mapping near-inertial variability in the SE Bay of Biscay from HF radar data and two offshore moored buoys, *Geophys. Res. Lett.*, *38*, L19607, doi:10.1029/2011GL048783.

Schott, F. (1971), Spatial structure of inertial-period motions in a two-layered sea, based on observations, *J. Mar. Res.*, *29*, 85–102.

Shay, L. K. (1997), Internal wave-driven surface currents from HF radar, *Oceanography*, *10*(2), 60–63.

Shay, L. K., T. N. Lee, E. J. Williams, H. C. Graber, and C. G. H. Rooth (1998), Effects of low-frequency current variability on near-inertial sub-mesoscale vortices, *J. Geophys. Res.*, *103*(C9), 18,691–18,714.

Stammer, D. (1997), Global characteristics of ocean variability estimated from regional TOPEX/POSEIDON altimeter measurements, *J. Phys. Oceanogr.*, *27*(8), 1743–1769.

Thomson, R. E., and W. S. Huggett (1981), Wind-driven inertial oscillation of large spatial coherence, *Atmos.-Ocean*, *19*(4), 281–306.

von Storch, H., and F. Zwiers (1999), *Statistical Analysis in Climate Research*, 484 pp., Cambridge Univ. Press, Cambridge, U. K.

Webster, I. (1968), Observations of inertial-period motions in the deep sea, *Rev. Geophys.*, *6*(4), 473–490, doi:10.1029/RG006i004p00473.

Weller, R. (1985), Near-surface velocity variability at inertial and subinertial frequencies in the vicinity of the California current, *J. Phys. Oceanogr.*, *15*(4), 372–385.

Zervakis, V., and M. Levine (1995), Near-inertial energy propagation from the mixed layer: Theoretical considerations, *J. Phys. Oceanogr.*, *25*(11), 2872–2889.

Zhai, X., R. Greatbatch, and J. Sheng (2005), Doppler-shifted inertial oscillations on a $\beta$-plane, *J. Phys. Oceanogr.*, *35*, 1480–1488.